

University of Massachusetts Amherst

**ScholarWorks@UMass Amherst**

---

Mechanical and Industrial Engineering Faculty  
Publication Series

Mechanical and Industrial Engineering

---

2021

## **Enhancing Light-Matter Interactions in MoS<sub>2</sub> by Copper Intercalation**

Chen Stern

Avraham Twitto

Rifael Z. Snitkoff

Yafit Fleger

Sabyasachi Saha

*See next page for additional authors*

Follow this and additional works at: [https://scholarworks.umass.edu/mie\\_faculty\\_pubs](https://scholarworks.umass.edu/mie_faculty_pubs)

---

---

**Authors**

Chen Stern, Avraham Twitto, Rifael Z. Snitkoff, Yafit Fleger, Sabyasachi Saha, Loukya Boddapati, Akash Jain, Mengjing Wang, Kristie J. Koski, Francis Leonard Deepak, Ashwin Ramasubramaniam, and Doron Naveh

---

# Enhancing Light–Matter Interactions in MoS<sub>2</sub> by Copper Intercalation

Chen Stern, Avraham Twitto, Rifaël Z. Snitkoff, Yafit Fleger, Sabyasachi Saha, Loukya Boddapati, Akash Jain, Mengjing Wang, Kristie J. Koski, Francis Leonard Deepak, Ashwin Ramasubramaniam, and Doron Naveh\*

The intercalation of layered compounds opens up a vast space of new host–guest hybrids, providing new routes for tuning the properties of materials. Here, it is shown that uniform and continuous layers of copper can be intercalated within the van der Waals gap of bulk MoS<sub>2</sub> resulting in a unique Cu–MoS<sub>2</sub> hybrid. The new Cu–MoS<sub>2</sub> hybrid, which remains semiconducting, possesses a unique plasmon resonance at an energy of  $\approx 1\text{eV}$ , giving rise to enhanced optoelectronic activity. Compared with high-performance MoS<sub>2</sub> photodetectors, copper-enhanced devices are superior in their spectral response, which extends into the infrared, and also in their total responsivity, which exceeds  $10^4\text{ A W}^{-1}$ . The Cu–MoS<sub>2</sub> hybrids hold promise for supplanting current night-vision technology with compact, advanced multicolor night vision.

of modern energy storage devices.<sup>[9,10]</sup> In some cases, the intercalation process is designed to modify the properties of the host material,<sup>[11]</sup> whereas in other cases, intercalation produces a continuous 2D material of interest, that would be hard to realize without the template of the confining environment of the vdW gap. For example, 2D gallium and indium that are grown by atomic intercalation at the interface of SiC and graphene, show potential for superconducting devices, topological phenomena, and advanced optoelectronic properties.<sup>[12]</sup> Another example of such intercalated layers are zero-valent metals and semiconductors, demonstrated in several host layered compounds.<sup>[13,14]</sup> In

the case of ionic intercalation, self-intercalation of Cu<sup>+1</sup> has improved the electronic transport in layered metal–chalcogen compounds.<sup>[15]</sup> These techniques have resulted in a vast array of chemically tunable behaviors including ambipolar optoelectronics in SnS<sub>2</sub>,<sup>[16]</sup> chemochromism in MoO<sub>3</sub>,<sup>[17]</sup> tunable enhanced transparency in Bi<sub>2</sub>Se<sub>3</sub>,<sup>[18,19]</sup> enhanced catalytic and energy storage behaviors in oxides,<sup>[20,21]</sup> tunable mechanical properties,<sup>[22]</sup> and enhanced thermoelectric performance in bismuth telluride.<sup>[23,24]</sup> The ability to chemically tune material


## 1. Introduction

Progress in the research of 2D layered compounds has continued at a sustained pace over the last decade with the discoveries of new compounds,<sup>[1,2]</sup> physical phenomena,<sup>[3,4]</sup> and technological advancements.<sup>[5,6]</sup> Intercalation chemistry in layered compounds, where the van der Waals (vdW) gap of the host compound is filled with guest (intercalant) atoms<sup>[7]</sup> or molecules,<sup>[8]</sup> is a cornerstone in many processes and forms the basis

C. Stern, A. Twitto, R. Z. Snitkoff, Prof. D. Naveh  
Faculty of Engineering  
Bar-Ilan University  
Ramat-Gan 52900, Israel  
E-mail: doron.naveh@biu.ac.il

C. Stern, A. Twitto, R. Z. Snitkoff, Dr. Y. Fleger, Prof. D. Naveh  
Institute for Nanotechnology and Advanced Materials  
Bar-Ilan University  
Ramat-Gan 52900, Israel

Dr. S. Saha, Dr. L. Boddapati, Dr. F. L. Deepak  
Nanostructured Materials Group  
International Iberian Nanotechnology Laboratory  
Avenida Mestre José Veiga s/n, Braga 4715-330, Portugal

 The ORCID identification number(s) for the author(s) of this article can be found under <https://doi.org/10.1002/adma.202008779>.

© 2021 The Authors. Advanced Materials published by Wiley-VCH GmbH. This is an open access article under the terms of the Creative Commons Attribution License, which permits use, distribution and reproduction in any medium, provided the original work is properly cited.

DOI: 10.1002/adma.202008779

Dr. S. Saha  
Electron Microscopy Group  
Defence Metallurgical Research Laboratory (DMRL)  
Hyderabad 500058, India

A. Jain  
Department of Chemical Engineering  
University of Massachusetts  
Amherst, MA 01003, USA

Dr. M. Wang, Prof. K. J. Koski  
Department of Chemistry  
University of California Davis  
Davis, CA 95616, USA

Prof. A. Ramasubramaniam  
Department of Mechanical and Industrial Engineering  
University of Massachusetts  
Amherst, MA 01003, USA

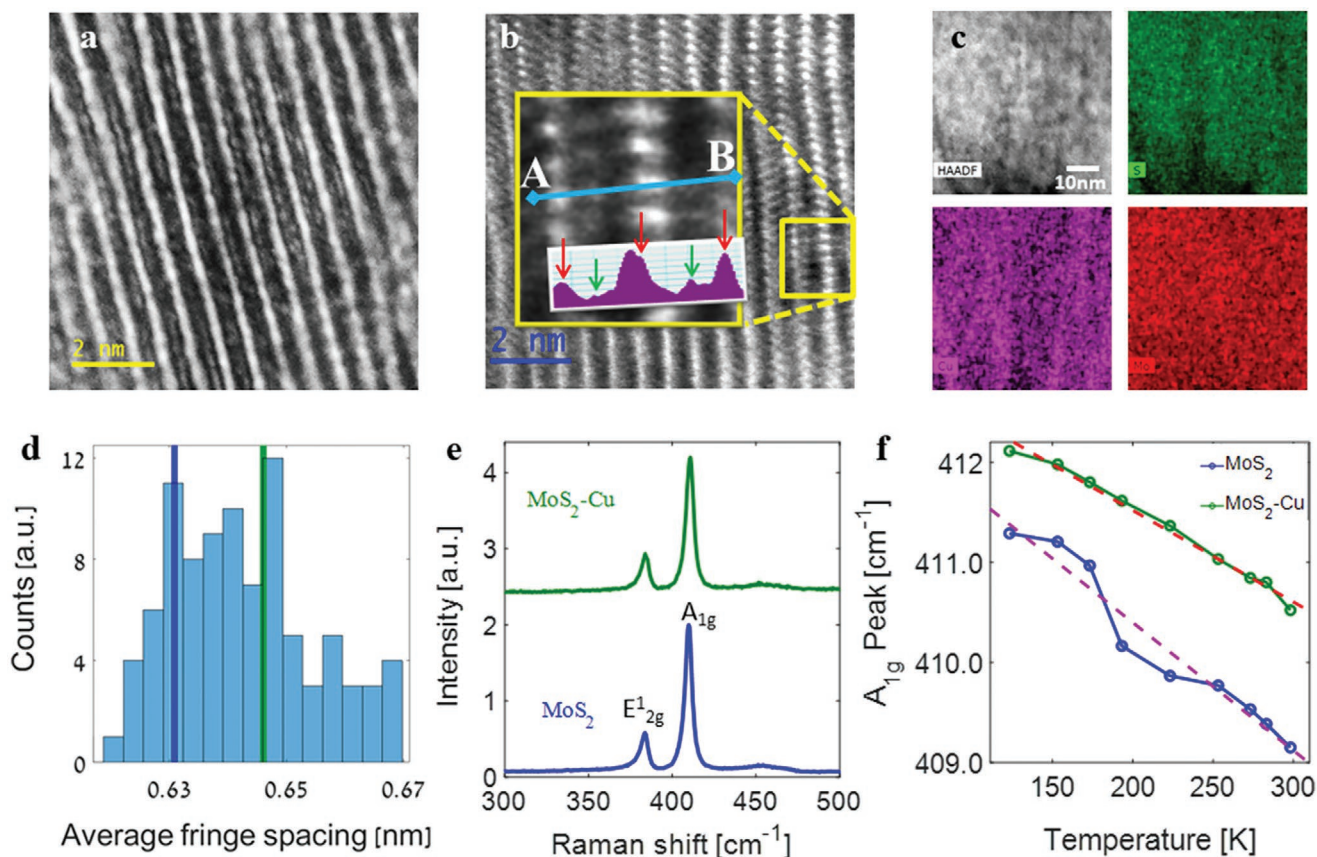


**Figure 1.** Structural characterization of VA-MoS<sub>2</sub> intercalated with zero-valent Cu atoms. a) HRTEM image displaying an additional layer due to intercalation of Cu within the vdW gaps. b) STEM-HAADF image showing a z-contrast image with the inset showing the magnified microscopy image of the area enclosed by the yellow square along with intensity profile along the line AB in the inset, with the layer of Mo-atoms appearing with higher intensity and Cu-atoms in between the layer of bright Mo-atoms, showing up with lower intensity. c) HAADF microscopy image along with elemental distribution maps collected from the energy-dispersive spectroscopy. d) Distribution and mean value of interlayer spacing between VA-MoS<sub>2</sub> planes before (blue line) and after (green line) Cu intercalation. e) Raman spectra of 2H-MoS<sub>2</sub> structure before (blue spectrum) and after (green spectrum) Cu intercalation. f) Temperature-dependent evolution of the peak of A<sub>1g</sub> Raman mode of MoS<sub>2</sub> before (blue) and after (green) Cu intercalation.

properties—including optical and electronic properties—through intercalation opens a vast space of new physical and chemical behaviors. As MoS<sub>2</sub> has already achieved significant interest for its sizable photoresponse, further intensifying light–matter interactions and amplifying the response in the near-infrared (NIR) is a very attractive goal. Here, we demonstrate intercalation of uniformly distributed planar layers of copper into devices of vertically aligned MoS<sub>2</sub> (VA-MoS<sub>2</sub>) grown by chemical vapor deposition (CVD).<sup>[25–27]</sup> The intercalated material remains semiconducting and displays an enhanced photoresponse that we attribute to a hybrid plasmon of Cu–MoS<sub>2</sub>. The Cu–MoS<sub>2</sub> devices show a broad spectral response with a maximum value of 10<sup>4</sup> A W<sup>-1</sup> and extending into the NIR range, enabling potential applications in compact, multicolor night-vision technology.

## 2. Results and Discussions

Cu–MoS<sub>2</sub> hybrids were prepared by zero-valent intercalation<sup>[28]</sup> on CVD-grown VA-MoS<sub>2</sub><sup>[27]</sup> (see Section 4 for details) followed by deposition of top indium tin oxide (ITO) contact

(see Figure 4), and a thin electron transparent lamella of the cross section of the device structure for inspection was prepared by the focused ion beam (FIB). The close-packed arrangement of copper atoms in MoS<sub>2</sub> host and their impact on the structure are inferred from the high-resolution transmission electron microscopy (HRTEM) and Raman spectra displayed in **Figure 1**. Figure 1a displays an HRTEM image of MoS<sub>2</sub> after intercalation of Cu atoms under the parallel beam illumination condition, showing the presence of fringe contrast coming from parallel sets of planes. The presence of an additional distinct layer within the vdW gap of MoS<sub>2</sub> suggests that copper atoms organize in close packing within the vdW space. The slight distortions of the layer planes (Figure 1a,b) are suggestive of some islanding of the copper within the host, consistent with a Daumas–Herold mechanism of intercalation.<sup>[29]</sup> The average interplanar spacing is found to be greater than the expected interplanar spacing for regular, intercalation-free MoS<sub>2</sub>, as seen from the distribution and mean value of the measured interlayer fringe spacing (Figure 1d). The average fringe spacing in the intercalated sample increases from 0.6309 to 0.6458 nm—an increase of 0.0149 nm. This layer expansion of 2.3% is significant and points to a substantial expansion of MoS<sub>2</sub>

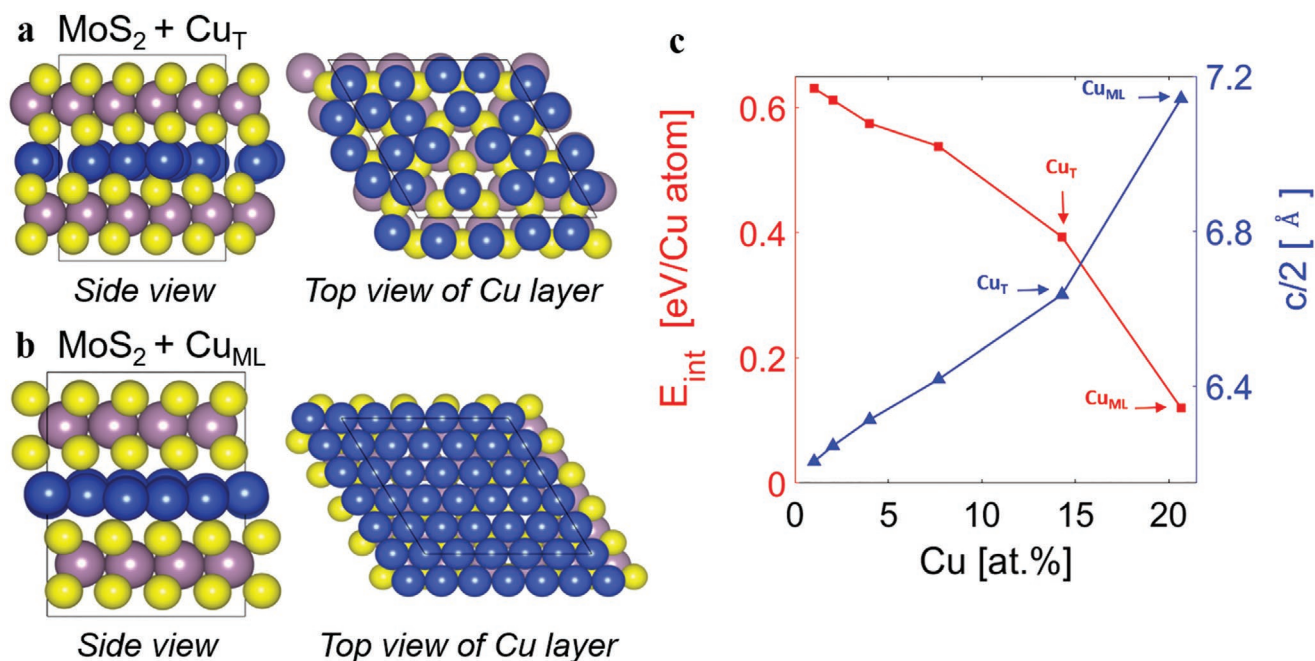


**Figure 2.** a,b) Structural models of a partial Cu layer ( $\text{Cu}_T$ ) (a) and a Cu(111) monolayer ( $\text{Cu}_{\text{ML}}$ ) (b) intercalated within a single vdW gap of bulk  $\text{MoS}_2$ . Unit cells are indicated by solid lines; one of the layers has been removed in the top views to show the intercalated Cu layers clearly. In (b), the supercell consists of a  $5 \times 5$  monolayer of Cu(111) which is nearly commensurate with a  $4 \times 4$  cell of  $\text{MoS}_2$ ; in (a) one Cu atom was initially inserted at every hollow site (between three S atoms) and allowed to relax, forming disordered 2D clusters. c) Energy per Cu atom ( $E_{\text{int}}$ ) required for intercalation into the vdW gap (red line) and the resulting interlayer separation ( $c/2$ ; blue line) both as functions of Cu concentration. Specific concentrations corresponding to the  $\text{Cu}_{\text{ML}}$  and  $\text{Cu}_T$  models are noted in the figure.

interlayer spacing due to Cu intercalation. This expansion is also illustrated in the high-magnification image in Figure 1a,b, which clearly shows the presence of an additional plane between two consecutive  $\text{MoS}_2$  (0002) planes. Figure 1c shows a high-angle annular dark-field scanning transmission electron microscopy (STEM-HAADF) image of a small region within the intercalated VA- $\text{MoS}_2$  sample and its corresponding colored TEM energy-dispersive X-ray spectrum (EDX) mapping of Cu. The Cu is found to be distributed throughout the host material. The presence of Cu in  $\text{MoS}_2$  is further confirmed from the Cu peaks seen in the EDS spectra (Figure S2, Supporting Information) acquired from the regions shown in Figure 1c. The copper concentration is found to be about 11 atomic percent, yielding a stoichiometry of  $\text{Cu}_{0.11}\text{MoS}_2$ .

After Cu intercalation there are now more conductive atoms within the host  $\text{MoS}_2$  structure that can play a key role in enhancing the electrical and optical properties, as discussed in detail later. Interestingly, the Raman spectra taken before and after intercalation show only small differences (Figure 1e). Spectra taken at a parallel geometry between the laser line and the  $c$ -axis of the crystal with linearly polarized light display the expected modes of 2H- $\text{MoS}_2$ , including an  $E_{2g}^1$  mode at  $\approx 383 \text{ cm}^{-1}$  that corresponds to an in-plane stretch and an  $A_{1g}$  mode at  $\approx 410 \text{ cm}^{-1}$  that corresponds to an out-of-plane breathing mode.<sup>[30]</sup> With intercalation of Cu,  $\text{MoS}_2$ , Raman modes show stiffening with an increase of  $\approx 2 \text{ cm}^{-1}$  for the  $A_{1g}$  mode (Figure 1f). The increase in the Raman wavenumber shift with intercalation is consistent with optical phonon stiffening and has been observed in other intercalated systems.<sup>[22,31]</sup> The thermal

coefficient of the  $A_{1g}$  mode of bare  $\text{MoS}_2$  ( $0.0127 \text{ cm}^{-1} \text{ K}^{-1}$ ) agrees well with previous reports.<sup>[32]</sup> The thermal coefficient of the Cu-intercalated samples ( $0.0091 \text{ cm}^{-1} \text{ K}^{-1}$ ) is  $\approx 28\%$  lower than the pristine  $\text{MoS}_2$ , and consequently the measured thermal conductivity decreases proportionally after the intercalation (see Supporting Information).<sup>[33]</sup>

Density functional theory (DFT) calculations were performed to gain further insights into the structural and electronic properties of the Cu-intercalated  $\text{MoS}_2$  structures. At low concentrations, intercalated Cu atoms bind to basal-plane sulfur atoms and are tetrahedrally coordinated.<sup>[34,35]</sup> With increasing concentration though, the Cu atoms tend to cluster spontaneously within the vdW gap (Figure 2a), ultimately forming slightly corrugated Cu (111) monolayers (Figure 2b). This computationally derived picture is in agreement with the experimental observations in Figure 1a,b, wherein we see partial to complete layers of Cu intercalated within the  $\text{MoS}_2$  vdW gap. The driving force for clustering can be quantified by the energetic cost of Cu intercalation (per atom),  $E_{\text{int}}$ , defined as

$$E_{\text{int}} = \frac{1}{n_x} (E_{\text{Cu}_x\text{MoS}_2} - E_{\text{MoS}_2} - n_x E_{\text{Cu,bulk}}) \quad (1)$$

where  $x$  is the atomic percentage of intercalated Cu in the  $\text{Cu}_x\text{MoS}_2$  structure and  $n_x$  is the total number of Cu atoms;  $E_{\text{Cu}_x\text{MoS}_2}$ ,  $E_{\text{MoS}_2}$ , and  $E_{\text{Cu,bulk}}$  are the 0 K DFT energies of  $\text{Cu}_x\text{MoS}_2$ , pristine  $\text{MoS}_2$ , and a single Cu atom (bulk FCC structure), respectively. As seen from Figure 2c, the intercalation energy progressively decreases with increasing Cu intercalation, going



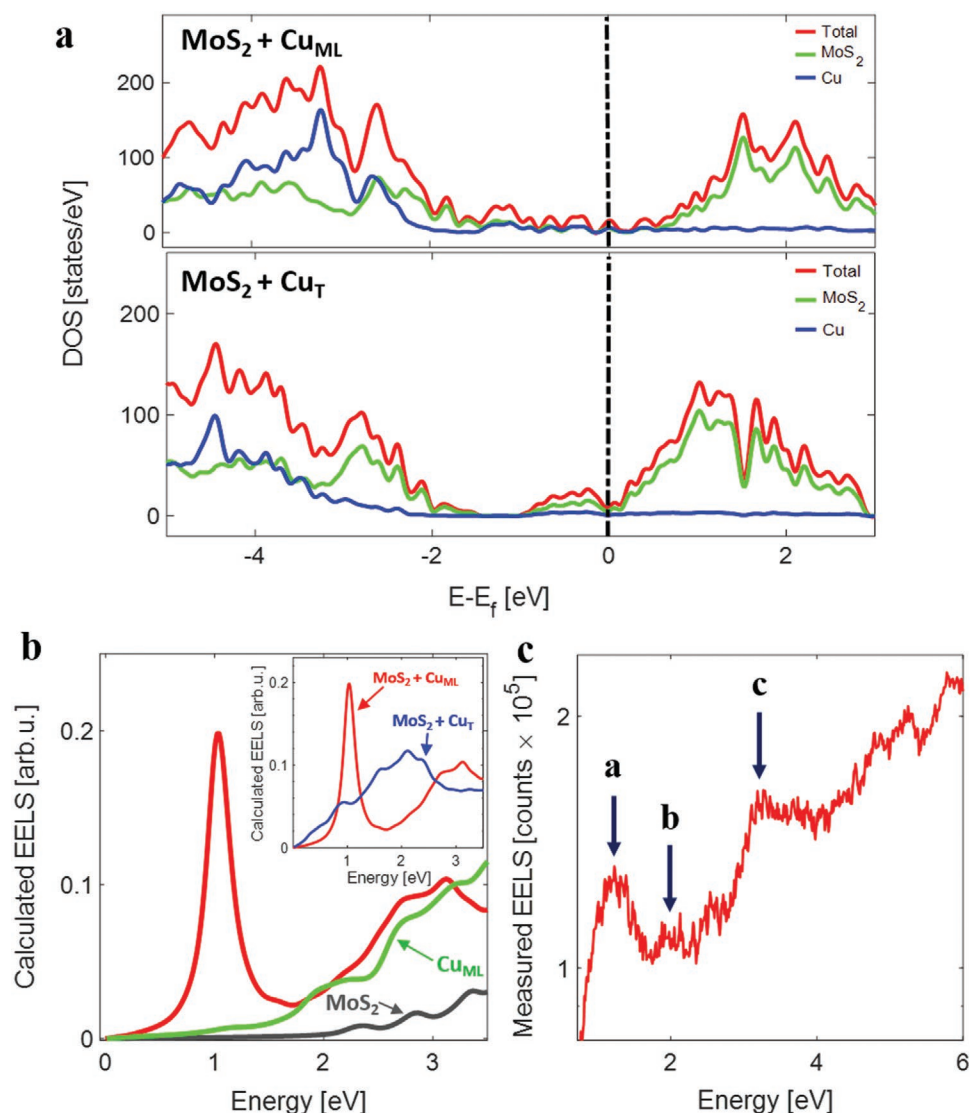


**Figure 3.** a) Density of states (DOS) of MoS<sub>2</sub> + Cu<sub>ML</sub> and MoS<sub>2</sub> + Cu<sub>T</sub> models calculated with the HSE functional; the total DOS (red lines) is further decomposed into contributions from MoS<sub>2</sub> (green lines) and Cu (blue lines). b) Calculated EELS spectrum of the MoS<sub>2</sub> + Cu<sub>T</sub> model (red line), bulk MoS<sub>2</sub> (gray line) and the isolated Cu<sub>ML</sub>; the inset compares the calculated EELS of the MoS<sub>2</sub> + Cu<sub>ML</sub> and MoS<sub>2</sub> + Cu<sub>T</sub> models. c) Low-loss EELS spectra obtained from the Cu-intercalated sample after removing the zero line peak.

from nearly 0.63 eV per atom for a single Cu atom to about 0.12 eV per atom for a complete monolayer. An intuitive physical picture for this observation may be proposed as follows. When Cu is intercalated into the vdW gap, there is an energetic cost associated with expanding the gap to accommodate the Cu atoms as well as an energetic cost associated with activating the fully coordinated, inert basal plane S atoms to form Cu–S bonds. Thus, the intercalation energy is initially high. With progressive Cu intercalation, first, the cost of destabilizing the vdW interaction between MoS<sub>2</sub> layers is partially compensated by interactions between clusters of Cu atoms (partial layers) and the MoS<sub>2</sub> layers. Second, and more important, as Cu atoms begin to cluster, we find that the number of Cu–S bonds are reduced and, consequently, the S atoms of the MoS<sub>2</sub> basal planes are less destabilized. The ultimate limit of a “cluster” is a complete Cu (111) monolayer, which only has weak chemical interac-

tions (bonding) with the MoS<sub>2</sub> layers but does have significant charge-transfer interactions, as will be discussed later. Finally, we also note the systematic expansion of the interlayer spacing (Figure 2c) from 6.17 Å in pristine MoS<sub>2</sub> to 7.14 Å for intercalation of a Cu monolayer. While this interlayer expansion is larger than in experiments, it should be noted that the DFT models allow for complete relaxation of the structure whereas, in practice, the VA-MoS<sub>2</sub> layers are confined by the Si wafer.

The electronic structures and optical properties of the Cu<sub>x</sub>MoS<sub>2</sub> models are displayed in Figure 3a,b. Upon examining the electronic density of states in Figure 3a, we find that the intercalated Cu introduces electronic states near the conduction band edge of MoS<sub>2</sub> and shifts the Fermi level close to the conduction band edge (*n* doping). At lower concentrations of intercalated Cu—associated with small clusters and some degree of Cu–S bonding—these additional electronic states form a broad

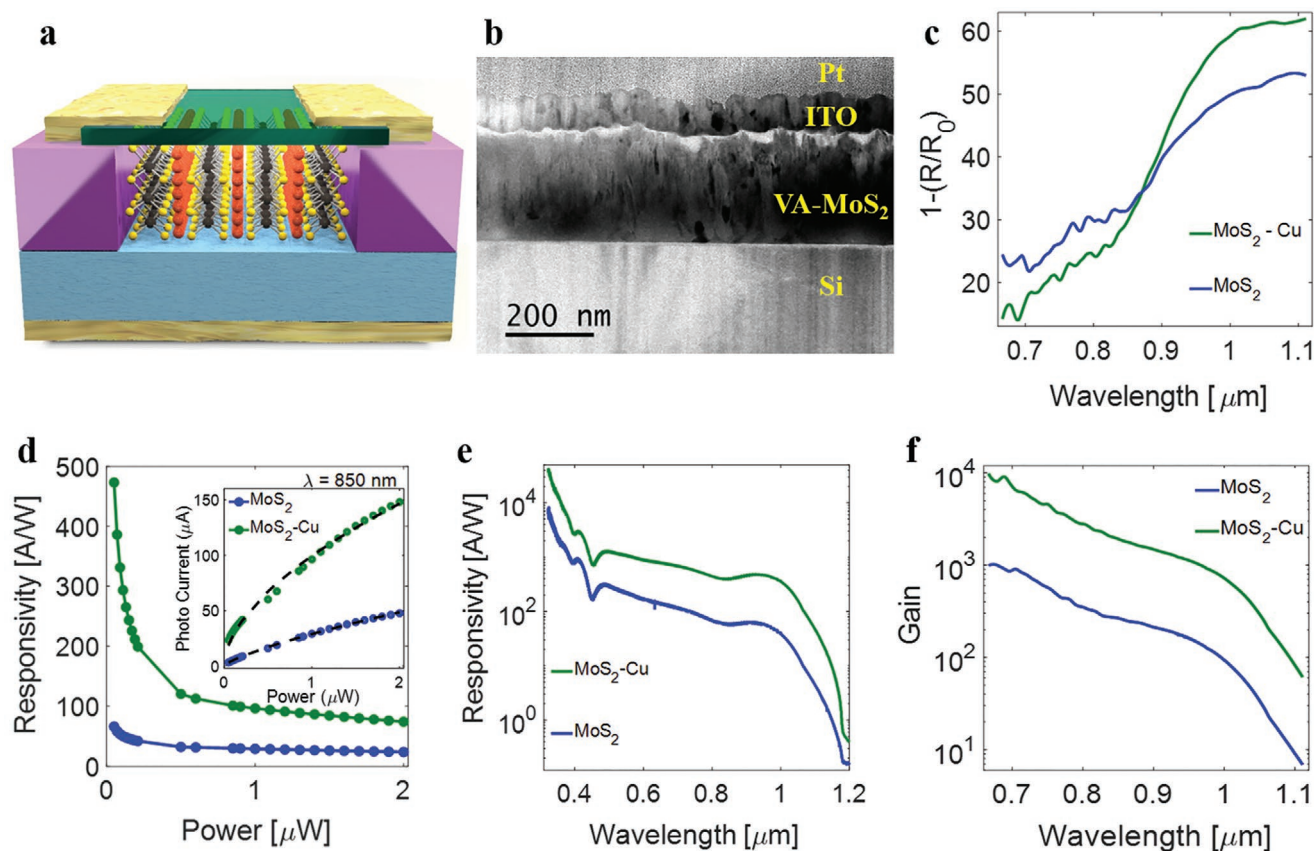
continuum near the conduction band edge; once the intercalated Cu forms a complete monolayer, these additional states appear as sharp resonances within the MoS<sub>2</sub> bandgap. The calculated EELS spectrum in Figure 3b reveals the emergence of a new plasmonic peak at ≈1.1 eV in the Cu-monolayer intercalated structures (MoS<sub>2</sub> + Cu<sub>ML</sub> model); this plasmon peak is not present either in bulk MoS<sub>2</sub> or in a Cu (111) monolayer, and is unique to the intercalated structure. Moreover, this sharp plasmon peak is not present in the partially intercalated structure (MoS<sub>2</sub> + Cu<sub>T</sub>), which only displays an overall enhancement in the electron energy loss spectroscopy (EELS) in the low-energy range (see inset of Figure 3b). We attribute the sharp plasmonic feature in the fully intercalated structure to optical transitions involving the numerous resonant gap states seen in Figure 3a. As the actual VA-MoS<sub>2</sub> samples consist of regions of complete, partial, or no Cu intercalation, the measured low-energy EELS spectrum is expected to reflect a weighted average of the calculated spectra from the partial and fully intercalated samples.

Figure 3c displays the measured low-loss EELS spectra from the Cu-intercalated MoS<sub>2</sub> sample and clearly reveals the emergence of new peaks plasmonic peaks as predicted by the density functional theory (DFT) calculations. The measured EELS spectrum displays three distinct peaks corresponding to: a) a hybrid MoS<sub>2</sub>-Cu excitation at ≈1.3eV in correspondence with the MoS<sub>2</sub>-Cu<sub>ML</sub> model; b) a smaller peak at ≈2 eV in correspondence with the MoS<sub>2</sub>-Cu<sub>T</sub> model; and c) a broad peak at ≈3.5 eV corresponding to the bare MoS<sub>2</sub>. The interpretation of the spectra, in conjunction with the DFT models, provides a picture wherein the intercalated Cu organizes within the vdW gap of MoS<sub>2</sub> in large (nearly continuous) domains as well as smaller patches. Intercalation, in general, can result in new EELS peaks from the appearance of new surface plasmons, bulk plasmons, or interband transitions. The optical doublet of MoS<sub>2</sub> from excitonic transitions<sup>[36,37]</sup> identified as A and B excitons, appears to be suppressed with intercalation. This suppression of optical modes has been observed in Cu-intercalated Bi<sub>2</sub>Se<sub>3</sub>.<sup>[38]</sup> The peak at ≈3eV is seen in MoS<sub>2</sub> and is attributed to excitonic transitions, specifically the C-exciton of MoS<sub>2</sub>.<sup>[36]</sup> This peak is attributed to transitions between the Γ-Λ point of the Brillouin zone<sup>[37]</sup> and does not vanish with Cu intercalation. The emergence of new plasmon peaks of intercalated metals, particularly copper, have been observed previously in other materials systems.<sup>[17,38]</sup> For example, a new EELS peak was seen at 4.3 eV in germanium-intercalated Si<sub>2</sub>Te<sub>3</sub> that was attributed to a new surface plasmon, bulk plasmon, or interband transition.<sup>[17]</sup> Cu intercalation in Si<sub>2</sub>Te<sub>3</sub> resulted in a shift of the bulk plasmon peak and the appearance of a new shoulder edge on the bulk plasmon peak.<sup>[31]</sup> Cu intercalation in solvothermally grown Bi<sub>2</sub>Se<sub>3</sub> also has shown the appearance of new plasmon modes and the broadening of existing peaks in the low-loss and higher regions.<sup>[38]</sup> Intrigued by the emergence of these new plasmons, we examine next the optoelectronic activity of the modified semiconductor, in particular, as photodiode devices.

Figure 4a displays a schematic representation of a Cu-intercalated VA-MoS<sub>2</sub> photodiode that comprises a Pd back contact to a P-Si wafer and an ITO top contact (see Section 4 for fabrication details). A cross-sectional TEM image of the device structure is displayed in Figure 4b. The microscopy image

clearly shows demarcations between the different layers present in the device structure: a layer of protective platinum on the top, which was deposited during the FIB sample preparation, followed by a layer of ITO, followed by the active layer of 70 nm VA-MoS<sub>2</sub> grown on the Si substrate. The total absorbance of the devices is displayed in Figure 4c. The bare MoS<sub>2</sub> device has optical absorptions between 20–50% over the range of 0.7–1.1 μm wavelengths respectively. Cu intercalation further enhances the NIR absorption of the device up to ≈60%. The photoresponse and photocurrent (at 850 nm) of VA-MoS<sub>2</sub> and Cu-intercalated VA-MoS<sub>2</sub> are displayed in Figure 4d,e, respectively. The responsivity of the MoS<sub>2</sub>/Si diode peaks at ≈ 66 A W<sup>-1</sup> whereas the responsivity of the Cu-intercalated device peaks at ≈500 A W<sup>-1</sup>. The responsivity of 66 A W<sup>-1</sup> is higher than most photodetectors based on MoS<sub>2</sub>/Si heterojunctions of this type.<sup>[39–45]</sup> Remarkably, intercalation of Cu improves the responsivity of the photodiode by an order of magnitude (Figure 4e) over a wide spectral range of ≈0.5–1.1 μm. At greater light intensities, the responsivity of the Cu-intercalated device decays<sup>[46]</sup> but still remains higher than that of the unintercalated device by a factor of three (Figure 4d).

The spectral response displayed in Figure 4e and the absorbance are related to the internal quantum efficiency (IQE),  $\eta_i$ , by the relation  $\eta_i(\lambda) = \frac{R(\lambda)hc}{\lambda\rho(\lambda)}$ , where  $\lambda$  is the wavelength of incident light,  $h$  is Planck's constant,  $c$  is the speed of light, and  $\rho(\lambda)$  is the absorbance;  $R(\lambda) = \frac{I_{ph}(\lambda)}{P(\lambda)}$  is the spectral responsivity, where  $I_{ph}(\lambda)$  is the photocurrent, and  $P(\lambda)$  is the power spectrum. Since the upper bound of IQE is 1, we attribute the excess of electrons collected per photon to a photoconductive gain. The gain (Figure 4f) at the 0.7–1.1 μm wavelength range attains peak values of ≈1000 and ≈10 000 for the pristine and Cu-intercalated devices, respectively. We attribute the high gain to defects in VA-MoS<sub>2</sub> that trap electrons for durations that are longer than the transit time of holes.<sup>[55]</sup> Table 1 outlines a comparative survey of Si-MoS<sub>2</sub> photodetector device performances. The maximum photoresponsivity of our devices ( $4.2 \times 10^4$  and  $8.2 \times 10^3$  for Cu:VA-MoS<sub>2</sub> and for the VA-MoS<sub>2</sub>, respectively) is found to be higher than most other devices. In addition to the responsivity peak value, the broad spectral response features high average values of 161 A W<sup>-1</sup> before and 830 A W<sup>-1</sup> after Cu intercalation, featuring a plateau in the spectral range of 500–847 nm. The Cu intercalation induces a photoconductive gain at a cost of some increase in response time; nevertheless, the photodetectors remain relatively fast (see Table 1). With the addition of Cu via intercalation, the additional gain is almost homogeneously distributed over the entire spectrum. Since the differences in optical absorption and electrical conductivity of the Cu-intercalated devices relative to bare MoS<sub>2</sub> are small, we attribute the photoresponse enhancement to the efficient ionization of zero-valent copper by photocarriers. This enhancement can be technologically beneficial for night-vision image intensifiers, working at low-light levels.<sup>[56]</sup> Traditionally, image intensifiers are based on intensifying tubes that convert scene photons to electrons on a photocathode; the electrons are multiplied via a multi-channel plate (MCP) and are accelerated to produce an enhanced image of the scene on a phosphorus screen. The intercalation-enhanced photodetectors may be



**Figure 4.** a) Graphical illustration of the cross-section of a VA-MoS<sub>2</sub> (yellow and black atoms)–Si (light blue) heterostructure photodiode device intercalated by Cu (red atoms). b) Cross-section transmission electron microscopy (TEM) image of the device. c) Absorption versus wavelength of the bare-MoS<sub>2</sub> device (blue) and the Cu-intercalated MoS<sub>2</sub> device (green). d) Responsivity as a function of incident power intensity of the bare-MoS<sub>2</sub> device (blue) and the Cu-intercalated MoS<sub>2</sub> device (green) under illumination of 850 nm at a reverse bias of –2 V. Inset: Dependence of photocurrent on incident power at wavelength of 850 nm. e) Responsivity versus wavelength of the bare-MoS<sub>2</sub> device (blue) and the Cu-intercalated MoS<sub>2</sub> device (green). f) Gain versus wavelength of the bare-MoS<sub>2</sub> device (blue) and the Cu-intercalated MoS<sub>2</sub> device (green).

**Table 1.** Comparison of the characteristics of Si–MoS<sub>2</sub> photodetectors reported in this work and those in previous reports.

Device	Responsivity [A W <sup>-1</sup> ]	Wavelength [nm]	Response time [rise/fall]	Ref.
Si/VA-MoS <sub>2</sub>	322.3–4.3	485–1100	5.2/1.2 μs	This work
	max: 8.26 × 10 <sup>3</sup>	325		
Si/Cu–VA-MoS <sub>2</sub>	1301–46	485–1100	16.7/11.2 μs	This work
	max: 4.2 × 10 <sup>4</sup>	323		
Si/VA-MoS <sub>2</sub>	8.75	580	10/19 μs	[39]
Si/VA-MoS <sub>2</sub>	0.3	808	3/40 μs	[40]
Si/VA-MoS <sub>2</sub>	0.908	808	56/825 ns	[41]
Si/VA-MoS <sub>2</sub>	7.37	532	—	[47]
Si/VA-MoS <sub>2</sub>	0.03	455	38.78/43.07	[48]
Si/VA-MoS <sub>2</sub>	0.654	980	2.1/173.8 μs	[49]
Si/VA-MoS <sub>2</sub>	49.31	800	80/79 ms	[50]
Single-layer MoS <sub>2</sub> FET	880	561	4/9 s	[51]
Si/single-layer MoS <sub>2</sub>	7.2	365	50/50 ms	[43]
Si/few-layers-MoS <sub>2</sub>	76.1	660	>50/48.9 s	[52]
Si/thin-film-MoS <sub>2</sub>	23.1	780	21.6/65.5 μs	[44]
Si/multilayer MoS <sub>2</sub>	11.9	650	30.5/71.6 μs	[53]
Si/MoS <sub>2</sub> Q.D.	2.8	514	—	[54]



good candidate technology for the core elements of vis to NIR image intensifiers, replacing bulky tubes with compact color vision. The high performance within the NIR part of the spectrum could allow for extra imaging capabilities under low-light (photon counting) scenarios, even on moonless nights due to the atmospheric night glow phenomena. In addition, the NIR band is most suitable for imaging and analysis of high vegetation terrain (e.g., forests, agricultural fields).

### 3. Conclusions

We have studied the impact of Cu intercalation on the electrical and optical properties of MoS<sub>2</sub> through a combination of materials characterization, theoretical calculations, and device measurements. Interestingly, Cu-intercalated MoS<sub>2</sub> remains semiconducting even at high densities of Cu intercalation. Structurally, intercalation results in a 2.3% expansion of the MoS<sub>2</sub> interlayer spacing, accompanied by stiffening of the Raman A<sub>1</sub> mode and higher thermal conductivity. The Cu-intercalated MoS<sub>2</sub> samples were implemented in fast, spectrally broad, highly responsive photodiodes. Relative to pristine MoS<sub>2</sub> devices, the Cu-intercalated devices showed over an order of magnitude enhancement in photoresponse over a range of 0.5–1.1 μm. With a photoconductive gain reaching 10 000, the devices are promising candidates for night-vision imaging, leading to significant improvements over the photomultiplier-phosphor plate technology.

### 4. Experimental Section

**Sample Preparation:** The fabrication of CVD-grown MoS<sub>2</sub>-Si diodes is described in detail in ref. [27]. Zero-valent Cu atoms were intercalated into the vdW gaps between the layers of VA-MoS<sub>2</sub> by a wet-chemical process.<sup>[13]</sup> Briefly, 0.01 g of tetrakisacetonitrile copper hexafluorophosphate (Millipore-Sigma) was added to 5 mL acetone (Millipore-Sigma) in a round-bottom flask attached to a Liebig reflux condenser. The solution was brought almost to reflux at 48 °C. The substrate was placed into the solution in the round-bottom flask. The solution was allowed to sit just below reflux for 4 h, whereupon it was removed and rinsed with acetone several times. ITO and metal contacts were finally deposited after patterning with e-beam lithography.

**Sample Characterization—Raman Spectroscopy:** Raman spectra were obtained using a Horiba Scientific Labram HR Evolution equipped using 532 nm solid state excitation laser and an optical microscope. The laser excitation propagated parallel to the crystal *c*-axis with linear polarization. A 50× objective lens was used to focus the laser and collect the Raman scattered light, and an 1800 lines per mm grating was chosen for spectrum acquisition.

**Sample Characterization—FIB, HRTEM, and STEM-EDS:** Site-specific, cross-sectional FIB prepared TEM lamellae were imaged using a Probe corrected FEI Titan G2 ChemiSTEM TEM equipped with a Super-X EDX system, which comprised four windowless silicon drift detectors of 120 mm<sup>2</sup> size, having an overall energy resolution better than 140 eV. The microscope was mounted with a Gatan 994 UltraScan 4K CCD camera, and the system had a point resolution better than 0.24 nm in the TEM mode and 80 pm in the STEM mode at 200kV accelerating voltage. The samples were imaged both in TEM and STEM modes as well as analyzed using STEM-EDS. To avoid any stray Cu signals in the EDS spectra, appropriate care was taken and molybdenum grids, rings, and clips were used for loading the sample in the TEM holder.

The EDS data were acquired and analyzed using the Bruker QUANTAX Esprit 1.9 software. The elemental quantification was performed using the Cliff–Lorimer method with the same software.

EELS was performed using a double-corrected FEI Titan Themis 60–300 kV equipped with a gun monochromator and a Gatan GIF Enfinity Fast dual EELS spectrometer, providing an energy spread of less than 0.19 eV at 60 kV. The spectra were acquired with an energy dispersion of 0.01 eV per channel, using 2.5 mm entrance aperture, and with 0.005 s exposure integrated over 2 s.

**Sample Characterization—Photoconductivity Measurements:** The monochromatic measurements were carried out at ambient conditions under illumination of a collimated 850 nm light-emitting diode (LED) (as discussed in the Supporting Information). Spectral responsivity and photocurrent were obtained by connecting the devices to an external detector socket of a Thermo Fisher Scientific Nicolet-iS50R. In order to obtain the Quartz-Halogen source black-body radiation curve, the source was measured using a DTGS detector. The device photocurrent spectrum was normalized to the source black-body curve to obtain the device's responsivity curve.

**Sample Characterization—Computational Methods:** Density functional theory (DFT) calculations were performed using the Vienna Ab initio Simulation Package (VASP; version 5.4.1).<sup>[57,58]</sup> Core and valence electrons were described using the projector-augmented wave method<sup>[59,60]</sup> and the Perdew–Burke–Ernzerhof generalized-gradient approximation<sup>[61]</sup> was used to describe electron exchange and correlation. The kinetic energy cutoff was set to 400 eV and Gaussian smearing of 0.05 eV was used for integrations over the Brillouin zone. The conjugate-gradient algorithm was used for structural optimizations of all DFT models with a tolerance of 0.01 eV per Å. During structural optimization, both atomic positions and cell vectors were relaxed. To model the intercalation of Cu atoms in bulk 2H-MoS<sub>2</sub>, 4 × 4 × 1 MoS<sub>2</sub> supercells were employed; this supercell was nearly commensurate with a 5 × 5 Cu (111) monolayer. The DFT-D3 method of Grimme et al.<sup>[62]</sup> was employed to include vdW interactions between MoS<sub>2</sub> layers. A sufficiently dense 4 × 4 × 3  $\Gamma$ -centered *k*-point mesh was used to sample the Brillouin zones of the supercells. As semilocal functionals underestimate fundamental gaps, the hybrid Heyd–Scuseria–Ernzerhof (HSE06)<sup>[63]</sup> functional was employed to calculate electronic structure and optical properties; PBE-relaxed Cu<sub>4</sub>MoS<sub>2</sub> structures were used in these calculations as the computational cost of structural relaxation with HSE is prohibitive.

### Supporting Information

Supporting Information is available from the Wiley Online Library or from the author.

### Acknowledgements

A.J. and A.R. gratefully acknowledge research funding from the U.S. National Science Foundation (NSF-BSF 1808011) and computational support from the Extreme Science and Engineering Discovery Environment (XSEDE), which is supported by National Science Foundation grant number ACI-1548562. D.N. would like to thank the Binational Science Foundation and U.S. National Science Foundation for jointly funding of this work with grant 2017655. The authors would like to thank Ilana Perelshtein for assistance with TEM imaging, Hadas Alon, Moshe Kirshner, and Mark Oksman for technical assistance. L.B. acknowledges the NanoTRAINforGrowth II program by the European Commission through the Horizon 2020 Marie Skłodowska Curie COFUND Programme (2015), and support provided by the International Iberian Nanotechnology Laboratory. F.L.D. would like to acknowledge the “Correlated Analysis of Inorganic Solar Cells in and outside an Electron Microscope (CASOLEM)” project (PTDC/NAN-MAT/28917/2017), co-funded by FCT and ERDF through COMPETE2020.

## Conflict of Interest

The authors declare no conflict of interest.

## Author Contributions

C.S. performed CVD growth; C.S. fabricated the devices; K.J.K. performed the intercalation process; C.S., R.S., and A.T. performed optical/electrical measurements; D.N., S.S., K.J.K., L.B., A.T., C.S., F.L.D. and R.S. analyzed the results; Under supervision of F.L.D., S.S. performed TEM/HRTEM, STEM-HAADF, EDS studies and LB performed monochromated-EELS measurements; A.T., R.S., and D.N. conducted the FTIR measurements; Y.F. performed FIB; A.R. and A.J. performed the theoretical calculations and simulations; D.N. conceived and supervised the study; all authors read and agreed with the manuscript.

## Data Availability Statement

The data that support the findings of this study are available from the corresponding author upon reasonable request.

## Keywords

copper intercalation, MoS<sub>2</sub>, photodetectors

Received: December 28, 2020

Revised: February 21, 2021

Published online:

- [7] M. Gibertini, M. Koperski, A. F. Morpurgo, K. S. Novoselov, *Nat. Nanotechnol.* **2019**, *14*, 408.
- [8] A. J. Mannix, B. Kiraly, M. C. Hersam, N. P. Guisinger, *Nat. Rev. Chem.* **2017**, *1*, 0014.
- [9] X. Huang, T. Wang, S. Miao, C. Wang, Z. Li, Z. Lian, T. Taniguchi, K. Watanabe, S. Okamoto, D. Xiao, S.-F. Shi, Y.-T. Cui, arXiv:2007.11155, **2020**.
- [10] Y. Cao, V. Fatemi, S. Fang, K. Watanabe, T. Taniguchi, E. Kaxiras, P. Jarillo-Herrero, *Nature* **2018**, *556*, 43.
- [11] X. Liu, M. C. Hersam, *Nat. Rev. Mater.* **2019**, *4*, 669.
- [12] H. Qiao, Z. Huang, X. Ren, S. Liu, Y. Zhang, X. Qi, H. Zhang, *Adv. Opt. Mater.* **2020**, *8*, 1900765.
- [13] G. L. Doll, J. S. Speck, G. Dresselhaus, M. S. Dresselhaus, K. Nakamura, S.-I. Tanuma, *J. Appl. Phys.* **1989**, *66*, 2554.
- [14] S. Jeong, D. Yoo, M. Ahn, P. Miró, T. Heine, J. Cheon, *Nat. Commun.* **2015**, *6*, 5763.
- [15] I. Samaras, S. I. Saikh, C. Julien, M. Balkanski, *Mater. Sci. Eng., B* **1989**, *3*, 209.
- [16] V. Shokhen, Y. Miroshnikov, G. Gershinsky, N. Gotlib, C. Stern, D. Naveh, D. Zitoun, *Sci. Rep.* **2017**, *7*, 3280.
- [17] X. Zhao, P. Song, C. Wang, A. C. Riis-Jensen, W. Fu, Y. Deng, D. Wan, L. Kang, S. Ning, J. Dan, T. Venkatesan, Z. Liu, W. Zhou, K. S. Thygesen, X. Luo, S. J. Pennycook, K. P. Loh, *Nature* **2020**, *581*, 171.
- [18] N. Briggs, B. Bersch, Y. Wang, J. Jiang, R. J. Koch, N. Nayir, K. Wang, M. Kolmer, W. Ko, A. De La Fuente Duran, S. Subramanian, C. Dong, J. Shallenberger, M. Fu, Q. Zou, Y.-W. Chuang, Z. Gai, A.-P. Li, A. Bostwick, C. Jozwiak, C.-Z. Chang, E. Rotenberg, J. Zhu, A. C. T. Van Duin, V. Crespi, J. A. Robinson, *Nat. Mater.* **2020**, *19*, 637.
- [19] K. J. Koski, J. J. Cha, B. W. Reed, C. D. Wessells, D. Kong, Y. Cui, *J. Am. Chem. Soc.* **2012**, *134*, 7584.
- [20] M. Wang, D. Williams, G. Lahti, S. Teshima, D. Dominguez Aguilar, R. Perry, K. J. Koski, *2D Mater.* **2018**, *5*, 045005.
- [21] X.-C. Liu, S. Zhao, X. Sun, L. Deng, X. Zou, Y. Hu, Y.-X. Wang, C.-W. Chu, J. Li, J. Wu, F.-S. Ke, P. M. Ajayan, *Sci. Adv.* **2020**, *6*, eaay4092.
- [22] Y. Gong, H. Yuan, C.-L. Wu, P. Tang, S.-Z. Yang, A. Yang, G. Li, B. Liu, J. Van De Groep, M. L. Brongersma, M. F. Chisholm, S.-C. Zhang, W. Zhou, Y. Cui, *Nat. Nanotechnol.* **2018**, *13*, 294.
- [23] M. Wang, K. J. Koski, *ACS Nano* **2015**, *9*, 3226.
- [24] J. Yao, K. J. Koski, W. Luo, J. J. Cha, L. Hu, D. Kong, V. K. Narasimhan, K. Huo, Y. Cui, *Nat. Commun.* **2014**, *5*, 5670.
- [25] M. Wang, I. Al-Dhahir, J. Appiah, K. J. Koski, *Chem. Mater.* **2017**, *29*, 1650.
- [26] A. C. Thenuwara, S. L. Shumlas, N. H. Attanayake, E. B. Cerkez, I. G. Mckendry, L. Frazer, E. Borguet, Q. Kang, M. J. Zdilla, J. Sun, D. R. Strongin, *Langmuir* **2015**, *31*, 12807.
- [27] C. Wu, H. Xie, D. Li, D. Liu, S. Ding, S. Tao, H. Chen, Q. Liu, S. Chen, W. Chu, B. Zhang, L. Song, *J. Phys. Chem. Lett.* **2018**, *9*, 817.
- [28] B. W. Reed, D. R. Williams, B. P. Moser, K. J. Koski, *Nano Lett.* **2019**, *19*, 4406.
- [29] L. Wu, J. Yang, M. Chi, S. Wang, P. Wei, W. Zhang, L. Chen, J. Yang, *Sci. Rep.* **2015**, *5*, 14319.
- [30] J. An, M.-K. Han, S.-J. Kim, *J. Solid State Chem.* **2019**, *270*, 407.
- [31] J. H. Yu, H. R. Lee, S. S. Hong, D. Kong, H.-W. Lee, H. Wang, F. Xiong, S. Wang, Y. Cui, *Nano Lett.* **2015**, *15*, 1031.
- [32] Y. Jung, J. Shen, Y. Liu, J. M. Woods, Y. Sun, J. J. Cha, *Nano Lett.* **2014**, *14*, 6842.
- [33] C. Stern, S. Grinvald, M. Kirshner, O. Sinai, M. Oksman, H. Alon, O. E. Meiron, M. Bar-Sadan, L. Houben, D. Naveh, *Sci. Rep.* **2018**, *8*, 16480.
- [34] J. P. Motter, K. J. Koski, Y. Cui, *Chem. Mater.* **2014**, *26*, 2313.
- [35] N. Daumas, A. Hérold, *C. R. Acad. Sci., Ser. C* **1969**, *268*, 373.
- [36] H. Li, Q. Zhang, C. C. R. Yap, B. K. Tay, T. H. T. Edwin, A. Olivier, D. Baillargeat, *Adv. Funct. Mater.* **2012**, *22*, 1385.
- [37] M. Wang, G. Lahti, D. Williams, K. J. Koski, *ACS Nano* **2018**, *12*, 6163.
- [38] N. A. Lanzillo, A. Glen Birdwell, M. Amani, F. J. Crowne, P. B. Shah, S. Najmaei, Z. Liu, P. M. Ajayan, J. Lou, M. Dubey, S. K. Nayak, T. P. O'regan, *Appl. Phys. Lett.* **2013**, *103*, 093102.
- [39] S. Sahoo, A. P. S. Gaur, M. Ahmadi, M. J.-F. Guinel, R. S. Katiyar, *J. Phys. Chem. C* **2013**, *117*, 9042.
- [40] Y. Han, M. C. Tringides, J. W. Evans, P. A. Thiel, *Phys. Rev. Res.* **2020**, *2*, 013182.
- [41] D. M. Guzman, N. Onofrio, A. Strachan, *J. Appl. Phys.* **2017**, *121*, 055703.
- [42] H. C. Nerl, K. T. Winther, F. S. Hage, K. S. Thygesen, L. Houben, C. Backes, J. N. Coleman, Q. M. Ramasse, V. Nicolosi, *npj 2D Mater. Appl.* **2017**, *1*, 2.
- [43] Y. Yu, Y. Yu, Y. Cai, W. Li, A. Gurarlan, H. Peelaers, D. E. Aspnes, C. G. Van De Walle, N. V. Nguyen, Y.-W. Zhang, L. Cao, *Sci. Rep.* **2015**, *5*, 16996.
- [44] J. J. Cha, K. J. Koski, K. C. Y. Huang, K. X. Wang, W. Luo, D. Kong, Z. Yu, S. Fan, M. L. Brongersma, Y. Cui, *Nano Lett.* **2013**, *13*, 5913.
- [45] V. Dhyani, S. Das, *Sci. Rep.* **2017**, *7*, 44243.
- [46] L. Wang, J. Jie, Z. Shao, Q. Zhang, X. Zhang, Y. Wang, Z. Sun, S.-T. Lee, *Adv. Funct. Mater.* **2015**, *25*, 2910.
- [47] S. Qiao, R. Cong, J. Liu, B. Liang, G. Fu, W. Yu, K. Ren, S. Wang, C. Pan, *J. Mater. Chem. C* **2018**, *6*, 3233.
- [48] J. Mao, Y. Yu, L. Wang, X. Zhang, Y. Wang, Z. Shao, J. Jie, *Adv. Sci.* **2016**, *3*, 1600018.
- [49] Y. Li, C.-Y. Xu, J.-Y. Wang, L. Zhen, *Sci. Rep.* **2014**, *4*, 7186.

- [44] Z. Lou, L. Zeng, Y. Wang, D. Wu, T. Xu, Z. Shi, Y. Tian, X. Li, Y. H. Tsang, *Opt. Lett.* **2017**, *42*, 3335.
- [45] V. Dhyani, P. Dwivedi, S. Dhanekar, S. Das, *Appl. Phys. Lett.* **2017**, *111*, 191107.
- [46] G. Konstantatos, M. Badioli, L. Gaudreau, J. Osmond, M. Bernechea, F. P. García de Arquer, F. Gatti, F. H. L. Koppens, *Nat. Nanotechnol.* **2012**, *7*, 363.
- [47] B. P. Majee, Bhawna, A. Singh, R. Prakash, A. K. Mishra, *J. Phys. Chem. Lett.* **2020**, *11*, 1268.
- [48] H.-S. Kim, M. D. Kumar, J. Kim, D. Lim, *Sens. Actuators, A* **2018**, *269*, 355.
- [49] L. Z. Hao, W. Gao, Y. J. Liu, Y. M. Liu, Z. D. Han, Q. Z. Xue, J. Zhu, *Phys. Chem. Chem. Phys.* **2016**, *18*, 1131.
- [50] A. V. Agrawal, M. Kumar, *Mater. Res. Express* **2019**, *6*, 115011.
- [51] O. Lopez-Sanchez, D. Lembke, M. Kayci, A. Radenovic, A. Kis, *Nat. Nanotechnol.* **2013**, *8*, 497.
- [52] G. H. Shin, J. Park, K. J. Lee, G.-B. Lee, H. B. Jeon, Y.-K. Choi, K. Yu, S.-Y. Choi, *ACS Appl. Mater. Interfaces* **2019**, *11*, 7626.
- [53] Y. Zhang, Y. Yu, L. Mi, H. Wang, Z. Zhu, Q. Wu, Y. Zhang, Y. Jiang, *Small* **2016**, *12*, 1062.
- [54] S. Mukherjee, R. Maiti, A. K. Katiyar, S. Das, S. K. Ray, *Sci. Rep.* **2016**, *6*, 29016.
- [55] F. Xia, H. Wang, D. Xiao, M. Dubey, A. Ramasubramaniam, *Nat. Photonics* **2014**, *8*, 899.
- [56] L. A. Bosch, *Proc. SPIE* **2000**, 4128.
- [57] G. Kresse, J. Furthmüller, *Phys. Rev. B* **1996**, *54*, 11169.
- [58] G. Kresse, J. Furthmüller, *Comput. Mater. Sci.* **1996**, *6*, 15.
- [59] P. E. Blöchl, *Phys. Rev. B* **1994**, *50*, 17953.
- [60] G. Kresse, D. Joubert, *Phys. Rev. B* **1999**, *59*, 1758.
- [61] J. P. Perdew, K. Burke, M. Ernzerhof, *Phys. Rev. Lett.* **1996**, *77*, 3865.
- [62] S. Grimme, J. Antony, S. Ehrlich, H. Krieg, *J. Chem. Phys.* **2010**, *132*, 154104.
- [63] A. V. Krukau, O. A. Vydrov, A. F. Izmaylov, G. E. Scuseria, *J. Chem. Phys.* **2006**, *125*, 224106.